3. RESULTS AND DISCUSSION

3.1. Chapter I: SOLAR RADIATION: Actual daily dose at different latitudes and seasons

Solar irradiance is the main variable affecting the efficacy of the SODIS process. The value of the maximum (fair-weather) solar incident radiation is a function of the day of the year and the latitude. However, actual incident radiation also depends on the weather conditions which are fluctuant and erratic. The scientific community has carried out several efforts to develop complex tools capable of predicting not only the maximum theoretical radiation intensity but also real radiation intensities using historical climatic data. Some solar disinfection treatments take a long exposure time, especially the inactivation of resistant microorganisms and the disinfection of large water volumes. Therefore, the calculation of cumulated daily radiation is preferable to estimating instant radiation intensities.

Chapter I presents a novel algorithm to easily predict the actual daily dose for varying latitudes and seasons. The results obtained in this chapter are discussed in detail in **Article 5.**

Algorithm

The developed algorithm to calculate the actual daily dose (G_{day}) is based on the application of **Eq. 3.1** for each wavelength (λ):

$$G_{day}(\lambda) = F_2 \cdot F_1 \cdot p^o_{sn}(\lambda) \cdot \tau_{DL} \qquad \textbf{Eq. 3.1}$$

where:

- p^o_{sn} is the incident spectral photon flux density of sunlight at solar noon and is a function of the day of the year and latitude.

- τ_{DL} is the day length. It can be calculated as a function of the day of the year and latitude between 60°S and 60°N.

- F_1 relates the cumulated incident radiation and the daily dose if the solar photon flux density corresponds to that at solar noon and is constant during the day length.

- F_2 relates the real and the maximum cumulated incident radiation.

Maximum cumulated radiation: F_1

The result of multiplying $p^o_{sn}(\lambda)$, τ_{DL}, and F_1 corresponds to the maximum cumulated radiation in a day $G_{day}(\lambda)$. In this sense, the product must match with the integration of the incident spectral photon flux density of sunlight $p^0(\lambda)$ over a 1-day time. Thus, the integration of $p^0(\lambda)$ was computed using the Solar Position Algorithm (SPA) from NREL ("National Renewable Energy Laboratory, Solar Position Algorithm| NREL.," 2022) for a latitude of 45°N at λ = 307.5 nm (EMW for the direct damage of phiX174 virus), considering the 15th day of each month. These same data were then optimised with **Eq. 3.1** to obtain the proportionality factor F_1, minimising the NRMSE between the SPA data and those predicted by the fit function. F_1 took a value of 0.43 with an NRMSE of 1%. The value of F_1 thus obtained means that the average photon flux density of sunlight during the whole day length is 43 % of the photon flux density peak at the solar noon (p^o_{sn} **(307.5** *nm)).* The excellent data fit suggests that this value of F_1 (referred to fair-weather conditions at 45°N) is consistent during the year.

The next step consists in verifying if the value of F_1 depends on the latitude or if, in contrast, F_1 = 0.43 obtained at φ = 45°N can be generalised. To do so, F_1 was validated with predictions of the cumulated radiation for latitudes from 60°S to 60°N, with a step of 5°. The solid symbols reported in **Fig. 3.1** represent the cumulated radiation referred to the 15th day of each month and calculated by integration using SPA data. The curves represent the predictions obtained with **Eq. 3.1,** by using F_1 =0.43. All the predictions showed a very good agreement, with errors less than 13% for latitudes between 55°S-55°N, and 22% and 18% for 60°S and 60°N, respectively. This result means that a constant value F_1 = 0.43 can be used over the whole year in the latitude belt between 60°S and 60°N.

Fig. 3.1: Fit for the daily dose during the year for a latitude of 45°N and validation of the procedure to calculate $G_{day}(\lambda)$ as a function of the latitude and the day of the year. A: Latitudes from 0° to 60°N with steps of 5°. B: Latitudes from 60°S to 0° with steps of 5°.

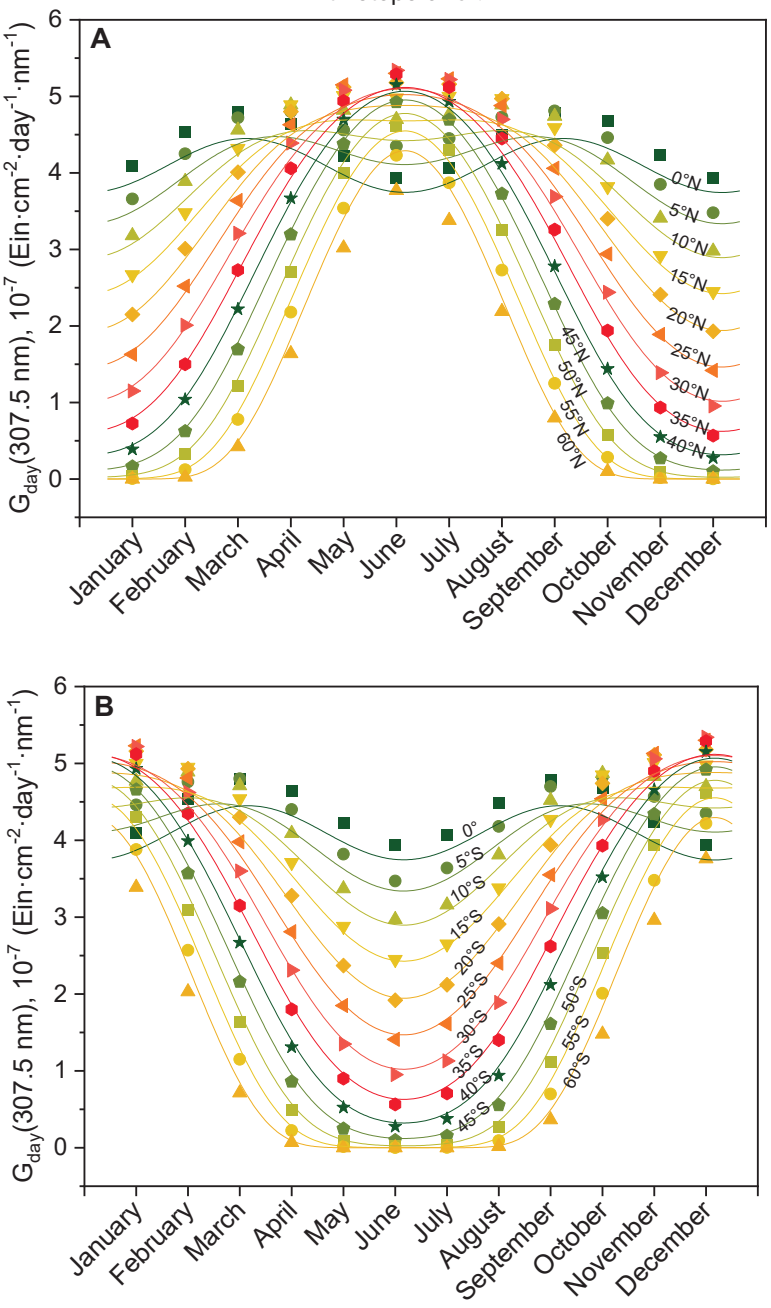

Actual cumulated radiation: F_2

The value of F_2 is variable even for the same location and day of the year since it depends on the weather conditions. This parameter can be calculated experimentally or estimated with historical data. It is strongly recommended to measure the actual irradiance in the field and calculate F_2 by dividing the experimental value by the theoretical value. However, if actual measurements are not available, F_2 can be estimated with historical data according to the procedure described by Moreno-SanSegundo *et al.* (2021). The values of F_2 as a function of the latitude and longitude geocoordinates are graphically available in **Fig. 3.2** and numerically in the Excel file (F_2.xlsx) provided as **SM** in **Article 5**.

Fig. 3.2: Worldwide representation of the annual average values of F_2 calculated from historical data of the last 12 years, based on the procedure developed by Moreno-SanSegundo *et al.* (2021).

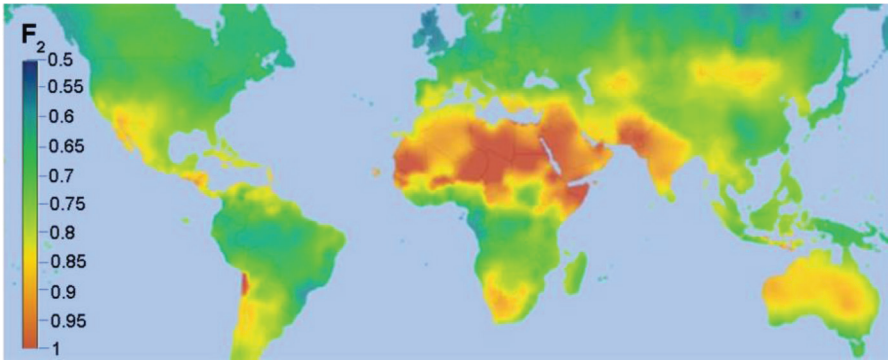

To evaluate F_2 accurately, predictions for the cumulated incident radiation calculated from 8.00 h to 16.00 h at 52°N latitude multiplying by the F_2 factor were compared to data from the literature (Frank and Klöpffer, 1988). In the cited paper, Frank and Klöpffer reported average radiation intensity (at 307.5 nm) referenced to the time interval of solar noon ± 4 h. To obtain the measured cumulated incident radiation, these values were multiplied by Δt = 28,800 s (i.e., the time interval from 8.00 h to 16.00 h). F_2 took a value of 0.58 (latitude 52°N, longitude 5°E). **Fig. 3.3** shows a good agreement between the predicted and literature data when using the estimated value of F_2 based on historical weather data, which reduces the NRMSE from 121% for F_2 = 1 to 25.5% for F_2 = 0.58. Therefore, an approach based on historical data of the weather considerably improves the prediction with respect to the assumption of fair-weather conditions.

Fig. 3.3: Comparison between literature (red squares, Frank and Klöpffer, 1988) and predicted data (*G*day*(307.5 nm),* green circles) of the cumulated radiation intensity.

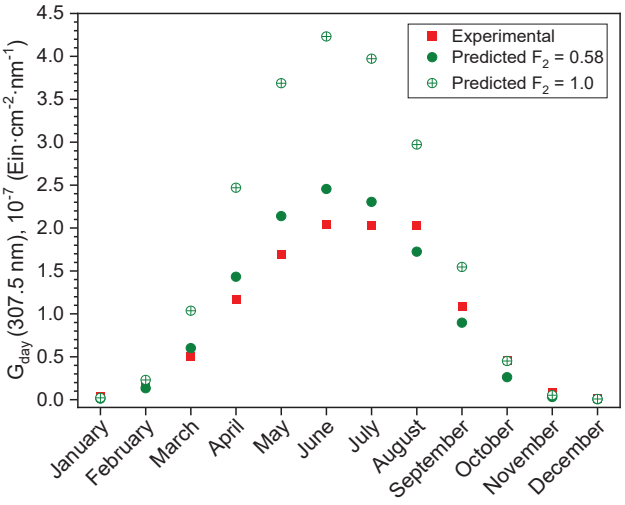

Final discussion

The developed algorithm can predict the actual daily dose depending on the latitude and day of the year. This algorithm has the following strengths:

- The simplicity of the procedure to estimate the actual daily dose around the world, with no need to use external and complex software.
- The possibility to calculate the actual daily dose for each wavelength, responding to different solar spectra. Validation for wavelengths other than 307.5 nm is recommended.
- The chance of coupling with the EMW approach, which estimates disinfection rates by considering only the actual daily dose for a single representative wavelength.

However, the simplicity of the procedure also leads to a few limitations:

- The loss of accuracy for disinfection treatments that take less than half a day of exposure time, as the evolution of the incident radiation throughout the day is approximately symmetrical with its maximum at midday.
- This procedure is not applicable for latitudes outside the 60°S-60°N latitude belt. However, for these extreme latitudes, the incident radiation received is usually not enough to take advantage of a sunlight-mediated process.

- Considering average weather with the F_2 factor may not predict well periods with consistently fine or bad weather. However, this is a limitation implicit to any other more complex prediction software.

3.2. Chapter II: CONTAINER MATERIAL: Material selection and prediction of solar irradiance in plastic devices

Generally, SODIS containers are manufactured with PET which cuts the transmission of UVB radiation. Therefore, the use of different plastic materials that allow transmission in the UVB range can significantly enhance disinfection rates. However, since SODIS is thought to be used by low-income populations, the employment of new materials must be affordable. At this point, SODIS container material should have good optical properties, but also good mechanical properties that clearly influence on the durability of the plastic container. Both properties are closely related to resistance to weathering, which, in the end, affects the durability/cost ratio and efficacy of the pathogens' inactivation process.

Chapter II presents a critical selection of the optimal plastic materials for SODIS containers, including the development of a tool to estimate the solar radiation available inside. The results obtained in this chapter are discussed in detail in **Article 1** and **Article 6.**

Preliminary material selection

Mechanical properties and production costs for PS, PVC, PE, PP, PC, PET, and PMMA plastics were exhaustively reviewed with data from the literature.

Table 3.1 summarises the results obtained from the revision. In conclusion, PP, PC, PMMA, and PET were selected as suitable candidate materials for manufacturing SODIS devices: PP showed low durability but can be well economically replaced and its lifetime can be extended adding UV-stabiliser, PET and PC presented moderate durability and production costs, and PMMA is an expensive plastic but relatively unaffected by photodegradation.

Regarding the optical properties, the transmission spectra of the four materials were experimentally analysed and are shown in Fig. 3.4. PC, PP, and PMMA allow transmission of UVB, UVA and visible radiation. The solar radiation reaching the Earth's surface only includes wavelengths above 290 nm. For these wavelengths, the transmittance is higher in the case of PMMA and, therefore, this plastic is better for manufacturing SODIS devices than PP, followed by PC. PET blocks UVB radiation transmission and, as a result, the viruses and protozoa inactivation is difficult (Busse *et al.,* 2019).

Table 3.1: Summary of mechanical properties and production costs for the selected plastic as candidate materials for manufacturing SODIS devices.

	Resistance	Photostability	Durability	Prod. costs
PS	Low	Low	Very low	
PVC	High	Low	Very low	
PE	High	Low	Very low	Very low
PP	High	Low	Low	Very low
PC	High	Moderate	Reasonable	Moderate
PET	High	Moderate	Reasonable	Moderate
PMMA	High	High	High	High

Fig. 3.4: Transmission spectra of PMMA, PP, PC, and PET.

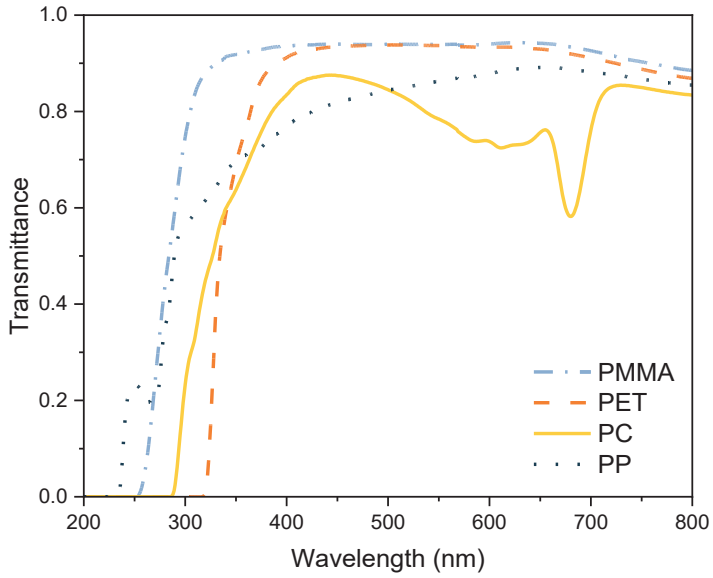

Impact of weathering on the lifetime of devices and disinfection efficacy

Due to the significant impact of weathering on SODIS devices, a deeper study was carried out through the accelerated ageing of plastics selected as suitable candidate materials and used in current SODIS processes: PMMA, PET, PP1 (PP with 1% by weight of UV-stabiliser), and PP2 (PP without UV-stabiliser).

The ageing of plastic materials due to weathering can affect both mechanical and optical properties, which leads to shorter lifetime and poorer disinfection

rates, respectively. **Table 3.2** summarises the main results obtained from the several techniques used to analyse mechanical properties and the estimated lifetime of SODIS devices manufactured with each plastic. In addition, **Table 3.2** also summarises the degradation of optical properties with ageing (measured as a loss of UVA and UVB transmittance). The effect of the decrease of radiation transmission on the disinfection efficacy was experimentally demonstrated with experiments of *E. coli* bacteria inactivation. **Fig. 3.5** depicts the evolution of the required solar exposure time to achieve 3 log reduction of *E. coli* bacteria with the ageing time for each plastic. Also, **Table 3.2** contains the variation of required time to achieve 3 log reduction for each plastic.

Table 3.2: Summary of the results obtained from the tests carried out to analyse the characteristics of the aged materials.

	PMMA	PET	PP1	PP2
Mechanical properties	Resistant but rigid	Hard and strong	Elastic up to 9M	Brittle after 2M
Durability	1 year at least	1 year at least	9 months	2 months
Tran. UVA	90%	60-30%	40%	40-25%
UVB	90-80%	0%	20-30%	20-0%
Disinfection time (3LR)	60-200 min	120-240 min	60-200 min	120-240 min

Fig. 3.5: Disinfection time to achieve 3-log reduction of *E. coli* for different solar exposure times and plastic containers.

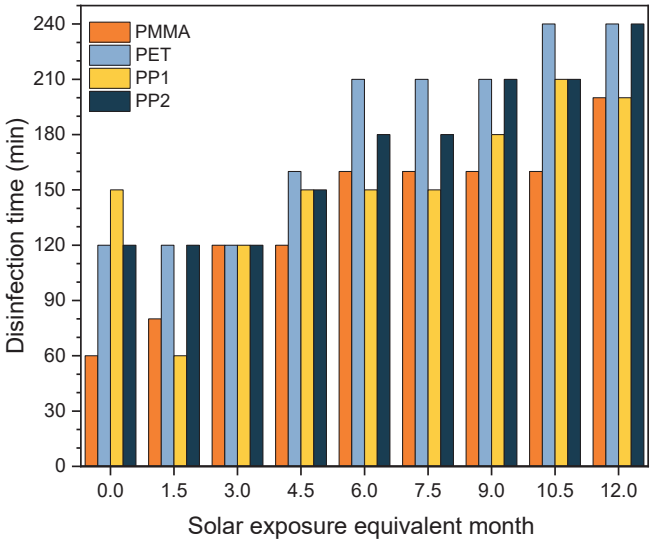

PMMA and PP with a 1% of UV-stabiliser were identified as excellent materials for manufacturing SODIS devices. PMMA proved to be a very photostable material with stable mechanical properties and a lifetime of more than one year. Also, it was demonstrated to have the best optical properties and disinfection rates. Although it is a resistant and rigid material, PMMA is easily scratched and, therefore, it is recommended for static (non-potable) SODIS devices. PP with a 1% by weight of UV-stabiliser retained stable optical properties with high disinfection rates and good mechanical properties without signs of significant degradation after 9 months of solar exposure. Since it is a plastic with good tensile strength and good impact resistance, it is recommended for portable SODIS devices. PET and PP without stabiliser were also analysed. Their disinfection rates were the lowest since PET does not transmit UVB radiation, and the transmittance of PP decayed due to the significant ageing of the plastic. The lifetime of PET was estimated, at least, as 1 year of solar exposure while only 2 months was reached for PP without additives.

***Solar UV Calculator* tool: Spectral irradiance available inside SODIS devices.**

SODIS mainly relies on damage caused to pathogens by solar UV radiation. However, the pathogen's sensitivity to photonic damage varies with the photon wavelength. Thus, the wavelengths transmitted into the interior of SODIS devices is a critical factor for disinfection performance. The *Solar UV Calculator* tool was developed to quantitatively estimate the available solar radiation and its spectral distribution inside a plastic SODIS container as a function of the plastic material and wall thickness (procedure described in **Section 2.3.2. *Solar UV Calculator* tool).** Two of its possible applications are: evaluating design parameters such as thickness and estimating experimental requirements such as solar exposure time.

The unlocked cells (input) allow to change:

- Material plastic of the device **(Fig. 3.6)**
- Thickness of the device **(Fig. 3.6)**
- Absorption spectra of a new material sample.
- Thickness of the new material sample.

The *Solar UV Calculator* returns:

- Numerical data and distribution (%) of the transmitted solar radiation for UVB, UVA, Visible ranges **(Fig. 3.6).**
- Graphical data of the spectral incident radiation outside and inside the device in the UV-Vis range.
- Graphical data of the transmittance spectra of the materials.

- Numerical data of the solar AM1.5 spectrum and transmitted solar radiation spectra within the device.

The tool offers default radiation spectra for PMMA, PET, PC, and PP. Nevertheless, the developed *Solar UV Calculator* tool is freely available (**SM** of **Article 1**) to any potential user interested in the evaluation of SODIS processes with other materials and conditions, or even to the evaluation of other solar processes subjected to a strong spectral dependence on materials transmission.

Fig. 3.6: Capture screen of the *Solar UV Calculator* tool. Top: Parameters design (thickness and plastic material) and numerical data and distribution (%) of the transmitted solar radiation. Bottom: Graphical data of the spectral incident radiation outside and inside the device in the UV-Vis range.

	Transmitted solar radiation (from Solar AM1.5 spectra)				
	Scenario 1	Scenario 2	Scenario 3	Scenario 4	Scenario 5
Thickness (mm)	2	1	2	2	2
Material	PP	PC	PET	PMMA	User
UVB (W/m^2)	0.29	0.68	-	1.45	0.00
UVA (W/m^2)	12.89	30.05	14.48	41.96	3.52
Visible (W/m^2)	287.88	424.25	341.61	506.46	191.16
UV-Vis (W/m^2)	301.07	454.97	356.10	549.87	194.68
UVB (%)	17.7	41.7	-	88.5	-
UVA (%)	28.3	65.9	31.8	92.0	7.7
Visible (%)	53.0	78.1	62.9	93.3	35.2
UV-Vis (%)	51.0	77.1	60.3	93.2	33.0
	Distribution of the transmitted solar radiation				
UVB/UV-Vis (%)	0.10	0.15	-	0.26	-
UVA/UV-Vis (%)	4.28	6.60	4.07	7.63	1.8
Vis/UV-Vis (%)	95.62	93.25	95.93	92.11	98.2

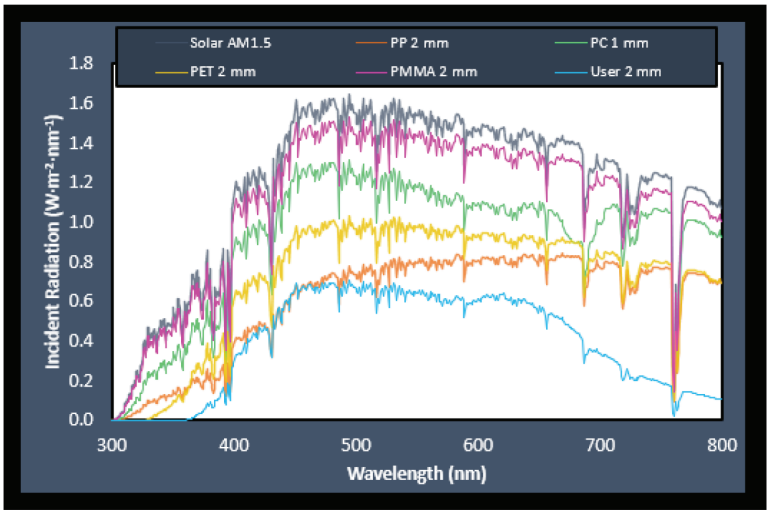

Final discussion

Regarding the selection of new plastic materials, the highlights are:

- The ageing of materials used in implemented SODIS processes demonstrated the necessity of studying the weathering of SODIS containers. Prolonged solar exposure can affect the efficacy of the process when the transmittance decays and the lifetime of the container is reduced as the plastic becomes brittle.

- Ideal mechanical properties are not crucial for selecting suitable materials if the material is used for non-portable SODIS devices or if the lifetime is balanced with costs (PMMA and PP, respectively). Indeed, PMMA and PP with a 1% UV-stabiliser were identified as excellent materials for manufacturing SODIS devices.

- PP with a 1% UV-stabiliser retained stable optical properties with high disinfection rates and good mechanical properties without signs of significant degradation after 9 months of solar exposure. Since it is a plastic with good tensile strength and good impact resistance, it is recommended for portable SODIS devices.

- PMMA proved to be a very photostable material with durable mechanical properties and a lifetime exceeding one year. Also, it demonstrated the best optical properties and disinfection rates. Although it is a resistant and rigid material, it is easily scratched, and it is recommended for static (nonportable) SODIS devices.

- PET and PP showed the lowest disinfection rates since PET does not transmit UVB radiation and the transmittance of PP decayed due to the significant ageing of the plastic. The lifetime of PET was estimated to be, at least, as 1 year of solar exposure while only 2 months for PP without additives.

- PS, PVC, and PE were ruled out as suitable materials for manufacturing SODIS containers because of their poor photostabilities.

Regarding the *Solar UV calculator,* this tool offers:

- The estimation of spectral irradiance inside SODIS containers manufactured with alternative plastic materials.

- The chance of evaluating different design parameters of SODIS containers such as the thickness and the type of material, or even other solar processes subjected to a strong spectral dependence.

- The possibility to study other materials if the absorption spectrum is known. This tool is freely available to any potential user.

- The opportunity to couple to a kinetic model to obtain the required solar exposure time based on design parameters.

3.3. Chapter III: WATER COMPOSITION: Naturally occurring substances as attenuating factors of radiation

SODIS is usually exposed in 2 L PET bottles. The limited volume of the bottles is a drawback as many small bottles working in parallel are required to provide sufficient quantity for a standard household. In Sub-Saharan Africa, 20-25 L plastic jerrycans are containers universally employed for water collection and transport. The use of transparent jerrycans could be an alternative and easy to implement HWT in this region. However, increasing the volume of the SODIS containers must be carefully addressed to ensure that the effect of water characteristics on the radiation distribution (transmission and scattering) is considered in order to make an in-depth appraisal of the required exposure time.

Chapter III presents a modelling approach of the SODIS process in large-volume containers that considers the effect of naturally occurring substances in water. The results obtained in this chapter are discussed in detail in **Article 2.**

Effect of naturally occurring substances in water

Bacterial inactivation experiments were carried out to check out the effect of the water composition on the SODIS process efficacy. Iron, solids, bicarbonates, soluble carbohydrates and humic acids were individually added to the water to assess the effect of common substances found in Sub-Saharan waters. Results were analysed based on the reduction of the viable bacteria count in comparison with unaltered water as a reference.

According to the results shown in **Fig. 3.7.A,** none of the substances enhanced the inactivation at the studied concentrations. A negligible effect was observed for the presence in water of bicarbonates and soluble carbohydrates. In contrast, the presence of iron, and especially of humic acids and solids showed a dramatic impact on the efficacy of the process. This effect can be attributed to the interference of the different substances in radiation transport which is confirmed by the transmission spectra in **Fig. 3.7.B.** In contrast, non-optically active substances (carbohydrates or bicarbonates) did not significantly affect the process.

Fig. 3.7: Effect of the presence of carbohydrates, bicarbonates, humic acids, iron, and solids: A) on the bacterial inactivation efficacy, B) on water transmission spectra.

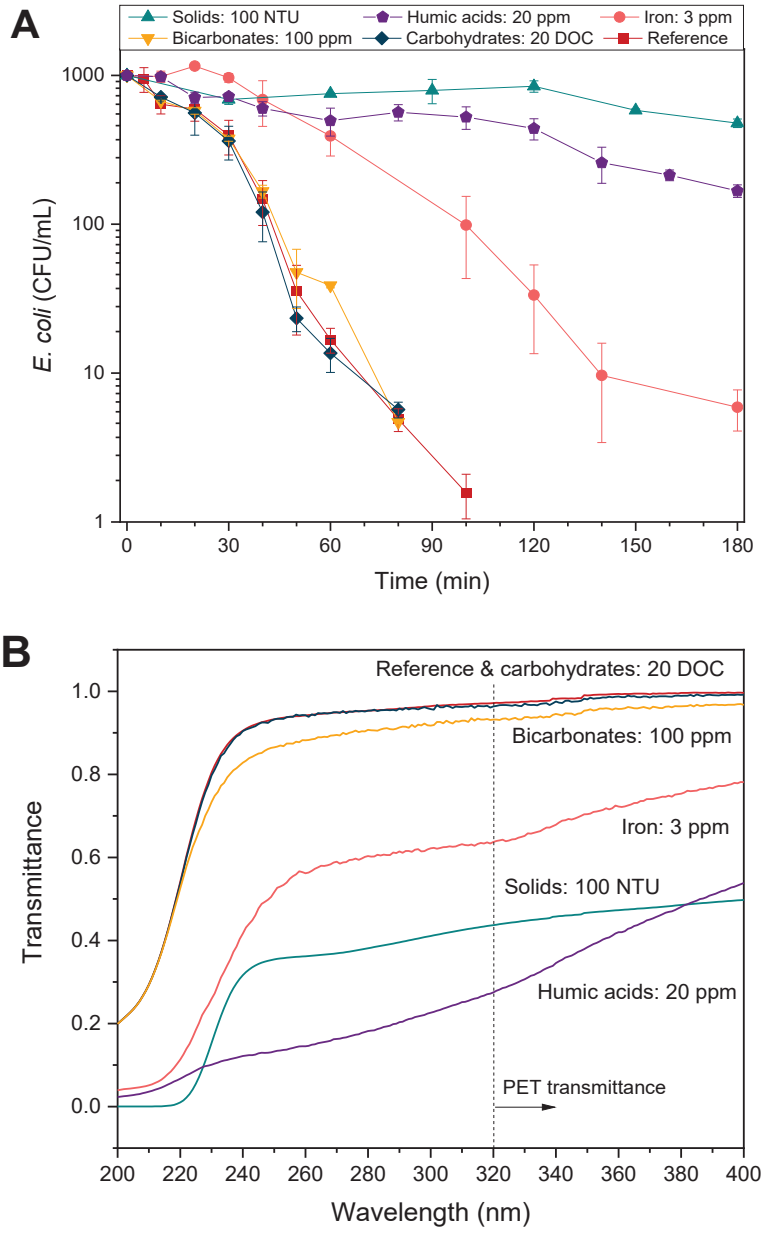

Optical properties of active substances

To analyse the correlation between radiation transfer and disinfection efficacy from a quantitative approach, the absorption (κ) and scattering (σ) coefficients and the *g* parameter of the Henyey-Greenstein scattering phase function of water with the different substances were determined experimentally **(Table 3.3).** In the case of solids, the attenuation is mainly due to radiation scattering, whereas for iron and humic acids the extinction is caused by photon absorption. As the radiation received by the bacteria decreases, more exposure time is required to achieve the same inactivation efficacy for the same level of irradiance. Therefore, in large-volume containers, the presence of solids, humic acids, and iron in water has a negative impact on the disinfection process because of their role as radiation attenuation factors. The effect of these optically active substances (iron, humic acid, and solids) was studied at different concentrations and UV irradiance values (11.3, 16.6, 21.6, and 28.2 W • m^{-2}) (experimental data shown in **Article 2).**

Table 3.3: Absorption (κ) and scattering (σ) coefficients and the *g* parameter of the Henyey-Greenstein scattering phase function for solids, dissolved iron, and humic acids.

	Solids (cm^{-1} • NTU^{-1})	Iron (cm^{-1} • ppm^{-1})	Humic Acids (cm^{-1} • ppm^{-1})
κ	$(2.40 \pm 2.00) \times 10^{-4}$	$(7.82 \pm 0.33) \times 10^{-2}$	$(1.20 \pm 0.28) \times 10^{-2}$
σ	$(7.39 \pm 0.21) \times 10^{-3}$	-	-
g	0.5246 (dimensionless)	-	-

Quantitative evaluation of radiation transfer in the container

The distribution of radiation within the container volume for increasing concentrations of the optically active substances was studied by means of numerical simulations of the radiation field developed in Ansys Fluent software **(Fig. 3.8.A** and **Fig. 3.8.B).** In addition, the average incident radiation and the uniformity index were calculated **(Table 3.4** and **Table 3.5).** Although in both cases a non-homogeneous distribution of radiation is observed (uniformity indexes lower than 1), significant differences appear depending on the absorption or scattering nature of the attenuation. Absorption by iron and humic acids **(Fig. 3.8.A)** led to a progressive decrease of incident radiation along with the container as the radiation pathway length increases, which means lower average incident radiation. In contrast, the scattering generated by the particles **(Fig. 3.8.B)** led to significantly more pronounced profiles with much higher values of incident radiation close to the front side, even above the irradiance, leading to a lower uniformity index. Experimental radiometric measurements at the rear of the container successfully validated the radiation modelling predictions.

Fig. 3.8: Distribution of the incident radiation (W • m^{-2}) in the longitudinal axis for a UVA irradiance in the front side (left in the plot) of 28.2 W • m^{-2} for different levels of iron and humic acids concentration (top) and turbidity (bottom).

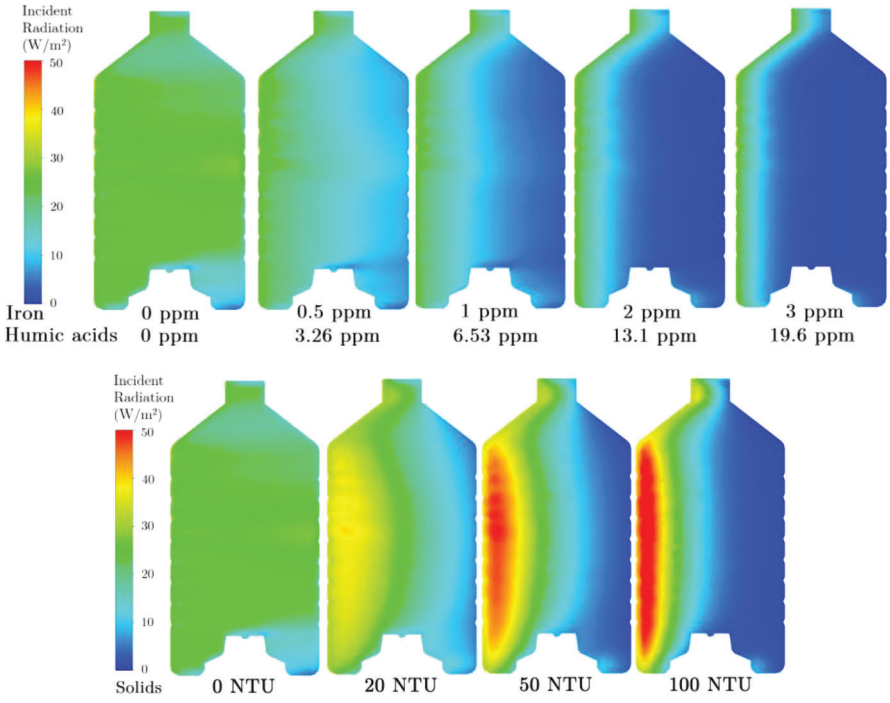

Table 3.4: Average incident radiation and uniformity index in the volume of the high-volume container as a function of iron or humic acids (HA) concentration.

Iron (ppm)/ HA (ppm)	0/ 0	0.5/ 3.26	1/ 6.53	2/ 13.1	3/ 19.6
G (W • m^{-2})	22.2	14.4	10.1	5.97	4.10
UI	0.94	0.86	0.76	0.59	0.49

Table 3.5: Average incident radiation and uniformity index in the volume of the high-volume container as a function of solids concentration.

Solids (NTU)	0	20	50	100
G (W • m^{-2})	22.2	20.7	17.3	12.8
UI	0.94	0.80	0.65	0.53

Effect on the *E. coli* inactivation kinetics

Considering the photoactivated nature of the bacterial inactivation process, the disinfection kinetic constant experimentally observed (k) should be proportional to the average incident radiation in the water volume (G), being k_0 the proportional kinetic factor (constant and radiation independent). In low-volume containers, differences in radiation distribution could be neglected due to the short optical path. In contrast, in large-volume containers, we found that not only the kinetics of the process is affected by the average value of the incident radiation, but also by the homogeneity in the distribution of the radiation. The integration of the uniformity index (UI) allows to consider the significant differences existing in the radiation distribution for similar values of G when the extinction is mainly produced by absorption or by scattering **(Eq. 3.2):**

$$k = k_0 \cdot G \cdot UI \qquad \textbf{Eq. 3.2}$$

Experiments in reference water (no substances added) at different radiation intensities were used to obtain k_0 and experiments in water with optically active substances were used as validation. **Fig. 3.9** shows the comparison of experimental and estimated first-order kinetic constant considering the model for low-volume containers ($k = k_0 \bullet G$, where $k_0 = 2.81 \bullet 10^{-3}$ m^2 • W^{-1} • min^{-1}, $R^2 = 0.999$) or large-volume containers (**Eq. 3.2,** where $k_0 = 2.99 \bullet 10^{-3}$ m^2 • W^{-1} • min^{-1}, $R^2 = 0.999$).

Fig. 3.9: Comparison of experimental first-order kinetic constant for *E. coli* photoinactivation and estimated by the kinetic model of radiation attenuating substances. A) kinetic model for low-volume containers, B) Kinetic model for high-volume containers.

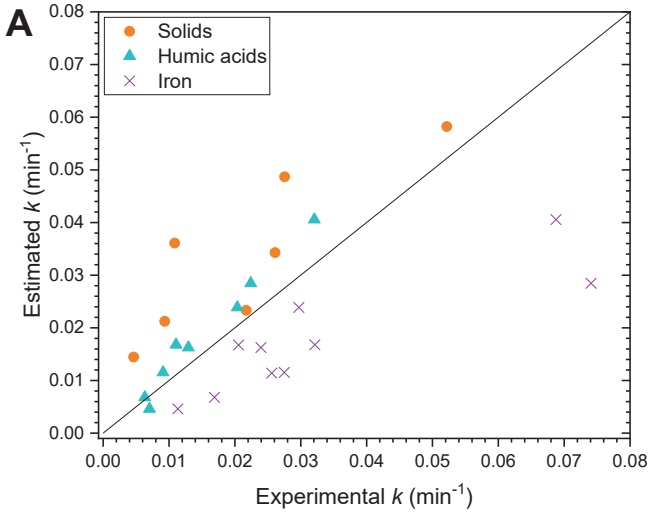

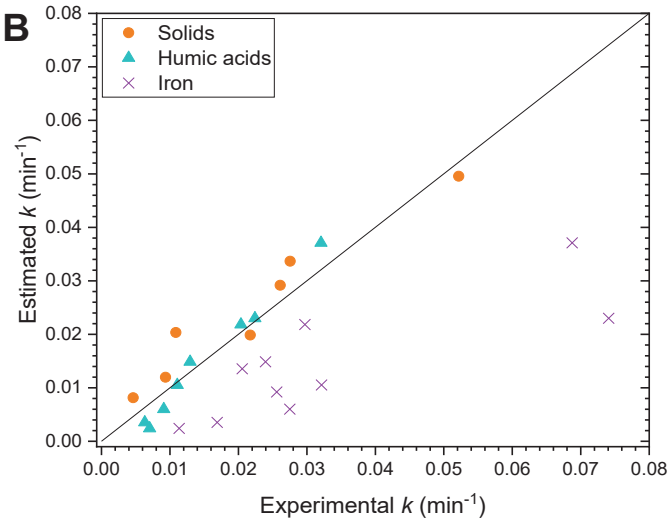

The consideration of the uniformity index reduced the error (calculated as NRMSE): from 66% to 22% for solids and from 31% to 20% for humic acids. In contrast, **Fig. 3.9.A** and **Fig. 3.9.B** shows that the values of the kinetic constants of experiments in the presence of iron were always higher than those estimated by the model (59% and 69% of NRMSE, respectively). The same optical properties and radiation distribution led to significantly different results when the absorption was produced by humic acids or iron. Kohantorabi *et al.* (2019) found that a concentration as low as 1 mg · L^{-1} of ferrous iron enhanced the disinfection rate since iron permeates into the cell and reacts with internal species to generate ROS that damage the bacteria (Kohantorabi *et al.*, 2019; Rommozzi et *al.*, 2020). These results observed in optically clear water and short optical path devices cannot be extrapolated to high-volume containers where the higher optical path length of the medium introduces radiation transport limitations. Consequently, whereas solids and humic acids has a negative effect on the efficacy of the solar disinfection process by their role as radiation attenuator, the effect of the presence of iron depends on a compromise between its detrimental role in the attenuation of radiation and its beneficial enhancement of the internal damage due to its permeation into the bacterial cell.

Final discussion

A novel procedure has been developed to calculate the available incident radiation in large-volume containers as a function of naturally occurring substances present in water using the average incident radiation and the uniformity

index values previously calculated using numerical simulation. The highlighted findings are:

- Applying the SODIS process in high-volume containers is feasible for a wide range of natural conditions.
- The required exposure time to achieve total bacterial inactivation is strongly dependent on water composition. The simulation of the radiation transport is critical since the strongly inhomogeneous distribution of radiation influences the disinfection rate (not only the average incident radiation).
- Absorptive substances (iron and humic acids) led to a progressive decrease of incident radiation along with the container as the radiation pathway length increases, while scatterer particles (turbidity) led to significantly more pronounced profiles with much higher values of incident radiation close to the front side, even above the irradiance, that means in lower uniformity index.
- The presence of optically active substances such as iron, humic acids, or solids was found to be an attenuating factor in large-volume containers where the potential role of external substances in the electron transport mechanism is completely overshadowed by the loss of radiation in the total volume of the container. In the case of iron, its permeation into the cells contributes to the intracellular Fenton process enhancing bacterial damage.
- The presence of substances transparent in the UV range such as bicarbonates and soluble carbohydrates has no impact on the disinfection rate.

3.4. Chapter IV: KINETIC MODELLING - VIRUSES: Mechanistic kinetic modelling of the thermal, spectral photonic, and synergistic effects

Following the standard procedure, 6 h of solar exposure are recommended to achieve solar water disinfection under sunny weather. However, due to the high variability of the numerous parameters involved in the process, this time is frequently overestimated. In the previous chapters, simple procedures have been developed to easily, but also accurately, estimate the spectral incident solar radiation reaching pathogens. The next and last step is the prediction of precise disinfection times to minimise solar exposure time, thus maximising safe drinking water production. To do so, the development of kinetic models is required. Due to their accuracy and rigour, mechanistic models have the

advantages of handling any operational conditions and describing the essential steps of the global process (here: thermal inactivation, direct and exogenous and endogenous indirect photoinactivation, and synergistic effects for the SODIS process). However, these steps are different depending, at least, on the type of pathogen. As far as pathogens causing waterborne diseases are concerned, viruses are the simplest because of their basic structure: just a genome surrounded by a protein capsid.

Chapter IV presents the development of a mechanistic kinetic model that considers the thermal, spectral photonic, and synergistic effects on virus solar disinfection in clear water. The results obtained in this chapter are discussed in detail in **Article 3.**

Dark thermal inactivation

No kinetic description was required for the dark inactivation since the experimental data recorded in the potential environmental temperature range (up to 50°C) showed negligible inactivation results. This is in agreement with Romero *et al.* (2011) who found that direct photolysis was responsible for solar inactivation of MS2 in the temperature range 14–42°C in the absence of external sensitisers.

UV irradiance and wavelength-dependent spectral action

In clear waters, indirect exogenous damage does not happen because of the lack of external sensitisers. In virus, the indirect endogenous damage mechanism can be neglected due to their simple structure of the microorganism. Therefore, photoinactivation of viruses in clear water can be reasonably assumed to occur mainly through direct endogenous damage based on the absorption of UVB solar radiation by the genome. This mechanism can be expressed by a first-order kinetic model (**Eq. 2.12**) where the kinetic constant can be defined as **Eq. 3.3** (see **Eq. 1.4**):

$$k_{endo} = \phi_v \int_{\lambda} \cdot \varepsilon_{RNA}(\lambda) \cdot [RNA]_v \cdot E(\lambda) \cdot d\lambda \qquad \textbf{Eq. 3.3}$$

where MS2 virus extinction coefficients ($\varepsilon_v(\lambda) = \varepsilon_{RNA}(\lambda) \bullet [RNA]_v$) were taken from the literature (Mattle *et al.,* 2015), spectral data of the incident light from 280 nm to 400 nm (radiation absorption of MS2 virus is negligible above 400 nm) were experimentally measured, and the quantum yield was calculated using experimental results. To do so, experimental data of the inactivation at 30°C (thermal effects can be neglected at 30°C) were fitted to a first-order

kinetic model **(Eq. 2.12)** and the kinetic constant was obtained using **Eq. 3.3.** The calculated quantum yield was ϕ_v = 2.07 · 10^{-3} viruses inactivated per absorbed photon (NRMSE = 11%).

Synergistic effect

Data from MS2 inactivation experiments under illuminated conditions (15, 20, 30, 40, and 50 W · m^{-2}) at different water temperatures (30, 40, 45, and 50°C) showed the clear effect of water temperature on photoinactivation rates at T > 40°C. This synergistic effect was included in the model by the temperature dependence of the kinetic constant according to the modified Arrhenius equation with a threshold (**Eq. 1.8** + **Eq. 1.9**) using a value of 40°C (313 K) for the temperature threshold (T_0). The quantum yield term in **Eq. 3.3** was redefined to include its dependence on below line math error (n = 423, $\phi_V^o = 2.15 \cdot 10^{-3}$ virus inactivated per absorbed photon and E_a/R = −1.30 · 10^5 K) was carried out by simultaneous fitting of the experimental data for the entire range of irradiances and temperatures with an NRMSE of 9.2%. **Fig. 3.10** depicts the comparison of the predicted and experimental kinetic constants showing excellent agreement.

Fig. 3.10: Agreement between observed and predicted kinetic constrants of the completed kinetic model.

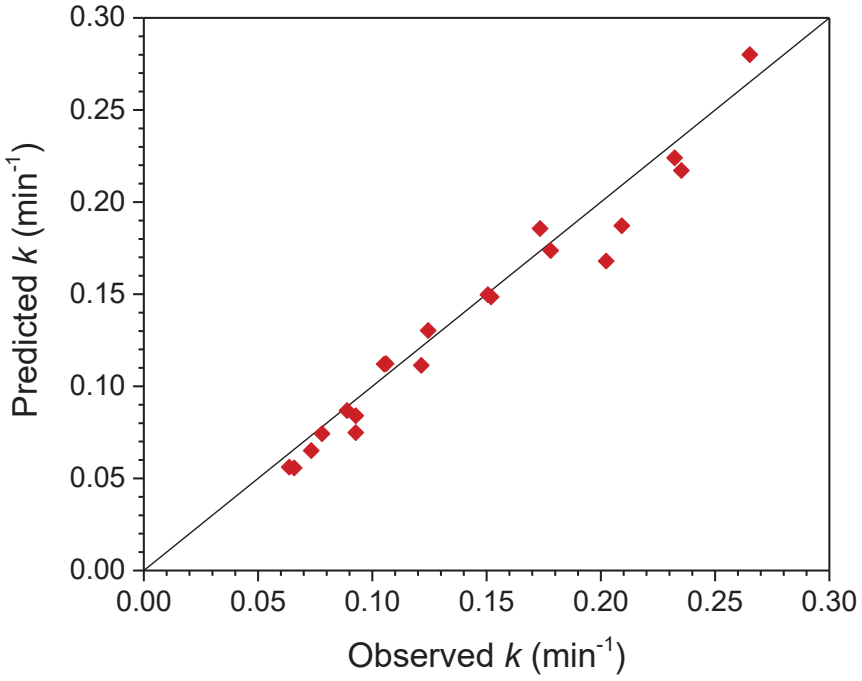

$$k = \phi_V^0 \left(\frac{T}{T_0} \right)^n \exp\left(-\frac{E_a}{R} \cdot \left(\frac{1}{T} - \frac{1}{T_0} \right) \right) \int_\lambda \varepsilon_v(\lambda) E(\lambda) d\lambda \qquad \textbf{Eq. 3.4}$$

Validation

The kinetic model was validated with a new set of experiments at different water temperatures, radiation intensities, and spectral distributions. To do so, different plastic samples were located between the reaction system and the radiation source, simulating that the process was performed in the PP and PPMA SODIS containers selected in **Chapter II** and the standard PET container (see **Fig. 3.6** in **Chapter II).** Note that, from now on, **PP1 (PP** with 1% by weight of UV-stabiliser) will be named just as **PP. Fig. 3.11** shows the comparison between the observed and predicted kinetic constants for PET, PP, and PMMA scenarios.

Fig. 3.11: Observed and predicted MS2 photoinactivation kinetic constant for experiments of validation using PP, PMMA, and PET to modify the spectral distribution of radiation.

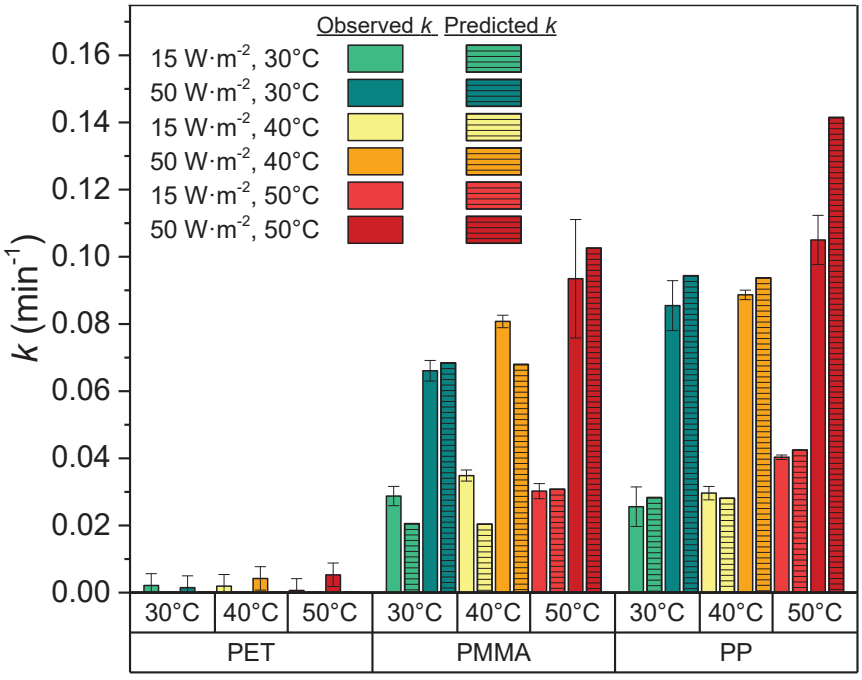

The agreement can be considered very good, with reasonable values of NRMSE of 28% and 18% for PP and PMMA, respectively. In the case of PET, the NRMSE is much higher (60%) due to the very low values of the inactivation rates (caused by low transmission in the UVB range). Thus, the UVB is the critical region where the virus absorption overlaps with the available solar incident radiation.

Model validation confirms the remarkable potential of the spectral-thermal synergistic model to predict MS2 photoinactivation with sunlight under different spectral and global irradiance values and temperatures around the world, specifically for the application of solar water disinfection processes with any type of container. In addition, the methodology and mathematical model presented can be easily extrapolated to other viruses with the obvious recalculation of specific kinetic parameters.

Final discussion

A novel comprehensive kinetic model for the MS2 virus inactivation has been developed as a function of the water temperature, irradiance, and spectral response of the virus. The highlighted findings are summarised as follows:

- Viruses showed no inactivation effect at natural water temperatures (20-50°C) under dark conditions.
- Viruses did show UV-T synergistic effect (under illumination conditions) at temperatures above 40°C, achieving 3-log reduction in 60-90 min.
- The model reproduces the expected biological spectral action according to the radiation absorption spectrum of the viral RNA, providing evidence for the lack of internal sensitisers, which would produce indirect endogenous photodamage.
- The model successfully responded to variations in the radiation spectrum, confirming the insignificant inactivation observed experimentally for PET, the most used material for SODIS processes.
- The lack of thermal inactivation under dark conditions and the single photoinactivation driven by UVB radiation demonstrated the necessity of using alternative materials different from PET, e.g. PMMA or PP with stabilisers, for manufacturing SODIS containers if viruses' inactivation is required.

In any case, application of the model to field conditions could require recalibration of the kinetic parameters to account for specific substances present in the water that could either enhance the process by acting as sensitisers for PPRI generation or diminish the efficacy by their role as radiation attenuators (this study was only carried out for bacterial inactivation in **Chapter III).**

3.5. Chapter V: KINETIC MODELLING - PROTOZOA: Mechanistic kinetic modelling of the thermal, spectral photonic, and synergistic effects

The more complex the pathogen structure, the more intricate the mechanistic kinetic model. Protozoa are single-celled eukaryotes, more resistant due to their complexity level. Indeed, some protozoa, such as *Cryptosporidium parvum,* can form cysts to survive unfavourable conditions. The great resistance of protozoa makes difficult their rapid photoinactivation. Thus, the accumulation of photodamage is required to achieve its removal. The mathematical description of these upgraded mechanisms results in more complex expressions.

Chapter V presents the development of a mechanistic kinetic model that considers the thermal, spectral photonic, and synergistic effects on protozoa solar disinfection in clear water. The results obtained in this chapter are discussed in detail in **Article 4.**

Dark thermal inactivation

Experimental results of inactivation in the dark at different water temperatures confirmed a noticeable effect of temperature above 30°C. Thus, this effect was modelled using a first-order kinetic model where the thermal inactivation kinetic constant is defined with the Arrhenius equation with a threshold temperature at 30°C (k_{T_0} = 1.12 × 10^{-4} h^{-1} and E_{aT}/R = 4.37 × 10^5 K, NRMSLE of 8.59%). However, these phenomena do not necessarily follow an Arrhenius behaviour. For this reason, the obtained kinetic parameters were not the final values, they were just used as seeds for the fit of the entire collection of experiments. The viability of *C. parvum* decreases progressively for temperatures in the range from 30 to 50°C due to the melting point of the fatty acids and hydrocarbons present in the oocyst wall and the increase in the metabolic activity (Fayer and Nerad, 1996; Jenkins *et al.,* 2010; King *et al.,* 2005; Peng *et al.,* 2008). Furthermore, temperatures above 37°C can induce the phenomenon of spontaneous excystation of *C. parvum*

oocysts, making their survival impossible in the absence of a host (Gómez-Couso *et al.,* 2009; Smith *et al.,* 2005).

UV irradiance inactivation

Solar inactivation of *C. parvum* is dominated by direct endogenous damage resulting from absorption of UVB radiation by the genome. Indirect endogenous damage is negligible since the action spectrum of *C. parvum* closely resembles that of the DNA absorption (Busse *et al.,* 2019; Liu *et al.,* 2015). Exogenous damage is also negligible since the presence of NOM, one of the most important external sensitisers, does not cause any effect on *C. parvum* viability, most likely due to its highly resistant thick oocyst wall (Liu *et al.,* 2015). Due to the presence of a shoulder in the experimental disinfection curves performed under illuminated conditions at 30°C, a series-event kinetic model was used. Calculation of the kinetic parameters (n = 8 and K_{RAD} = 4.05 × I0^{-2} m^2 • W^{-1} • h^{-1}) was carried out by fitting the experimental data, resulting in an NRMSLE of 2.44%. No recovery kinetic constant was required to fit the experimental results.

Synergistic effect

The coupling of the dark thermal inactivation model with the UV irradiance model to predict the inactivation of *C. parvum* failed at temperatures higher than 30°C (NRMSLE = 17.9%). The predictions clearly underestimate the experimental data, showing a higher error for higher temperatures, which supports the existence of a synergy between the thermal and photonic inactivation processes (Kevin G. McGuigan *et al.,* 1998; Wegelin *et al.,* 1994). The synergistic effect was included in the model through the temperature dependence of the kinetic constant of the series-event model according to the modified Arrhenius equation, using a value of 30°C for the temperature threshold again. All the kinetic parameters were recalculated using the provisional values in the previous submodels as seeds. The global fitting of the whole experimental data set for the complete range of irradiances and temperatures provides the values of the final kinetic parameters: n = 7, K_{RAD_o} = 2.97 × I0^{-2} m^2 • W^{-1} • h^{-1}, $E_{a_{RAD}}/R$ = 6.90 × IO^4 K, k_{T_0} = 4.19 × I0^{-5} h^{-1}, and E_{a_T}/R = 5.06 × I0^5 K with an NRMSLE of 3.68% **(Fig. 3.12).** Now, whereas the predictions of the dark thermal inactivation and the photoinactivation at 30°C are very similar to those obtained previously, the prediction of the photoinactivation at higher temperatures improves significantly.

Fig. 3.12: Observed and predicted photoinactivation profiles of *C. parvum* oocysts.

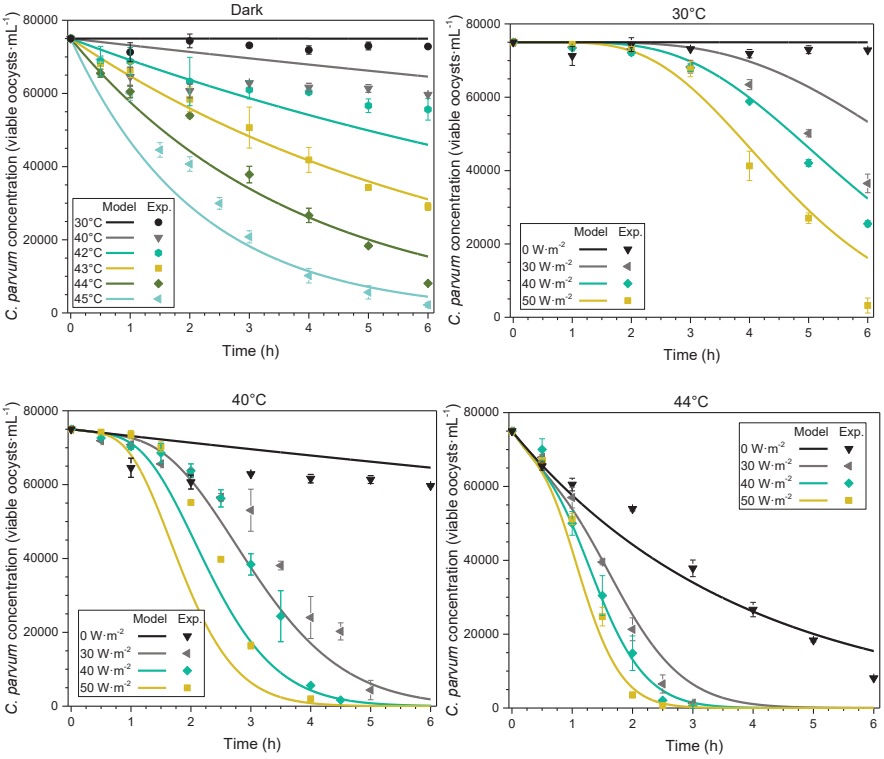

Wavelength-dependent spectral action

The inactivation kinetic constant can be calculated by multiplying the quantum yield by the volumetric rate of photon absorption as follows:

$$k_{endo} = \phi_{CP} \int_{\lambda} \varepsilon_{DNA}(\lambda) \cdot [DNA]_{CP} \cdot E(\lambda) \cdot d\lambda \qquad \textbf{Eq. 3.5}$$

C. parvum extinction coefficients (ε_{CP} (λ)) and the spectral irradiance *E(λ)* from 280 to 400 nm for a global UV of 50 W • m^{-2} can be found in the **SM** of **Article 4**. Following **Eq. 3.5,** the quantum yield for *C. parvum* inactivation was calculated as ϕ_{CP} = 3.94 × 10^{-7} oocysts damaged per absorbed photon, indicating that *C. parvum* is more resistant to direct inactivation than viruses such as phiX174, MS2, and adenovirus (1.4 × 10^{-2}, 2.9 × 10^{-3}, and 2.5 × 10^{-4} virus inactivated/absorbed photon, respectively) (Mattle *et al.,* 2015).

Validation

The kinetic model was validated with a new set of experiments at different water temperatures, radiation intensities, and spectral distributions. To do so, the same procedure used to validate the kinetic model for viruses was applied: PET, PPMA, and PP plastic samples were located between the reaction system and the radiation source. **Fig. 3.13** shows the comparison between the observed and the predicted inactivation profiles for the three scenarios.

Fig. 3.13: Observed and predicted inactivation profiles of *C. parvum* oocysts at different conditions of radiation intensities, radiation spectral distribution and water temperatures.

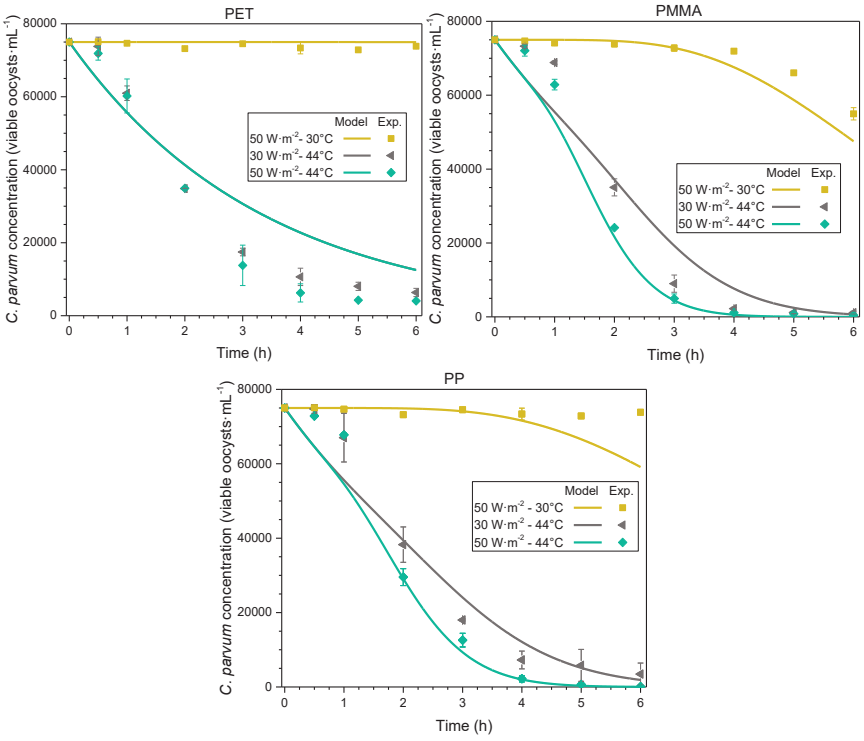

Considering the fully predictive nature of the model inactivation curves (they are not fitting results), the agreement can be considered very good with values of NRMSLE of 5.54, 5.72, and 11.68% for PET, PP, and PMMA, respectively. The results can be easily interpreted based on the different UV transmission of the materials obtained with the *Solar UV Calculator* tool: 1%, 44%, and 57% in the global UVB range, and 59%, 60%, and 86% in the UVA range, for PET, PP, and PMMA, respectively.

For the PP and PMMA scenarios, the thermal effect and the irradiance effect can be observed for experiments at the same global UV irradiance and the same water temperature, respectively. In the case of PET, a plastic that essentially does not transmit UVB radiation, the thermal contribution is almost the only damage source. As a result, the same disinfection rates for different values of global UV irradiance (i.e., 30 and 50 W • m^{-2} at 44°C) are achieved. The absence of external sensitisers and the negligible inactivation with only UVA and visible radiation at 30°C confirm two things: the threshold on the thermal inactivation set to 30°C and the dominant mechanism of *C. parvum* photoinactivation by the direct damage caused by the UVB photons' absorption by DNA. Thus, it also means that the thermal mechanism is the only pathway to inactivate *C. parvum* in standard SODIS PET containers. However, the temperature reached during solar water disinfection is easily raises above 30°C (Dejung *et al.,* 2007; Gómez-Couso *et al.,* 2010).

Final discussion

A novel comprehensive kinetic model for the *C. parvum* protozoon inactivation has been developed as a function of the water temperature, irradiance, and spectral response of the protozoon. The highlighted findings are summarised as follows:

- Protozoa showed thermal inactivation (under dark conditions) above 30°C and especially significant above 40°C, achieving 3-log reduction in 17 h at 44°C and in approximately 1 h at 50°C.
- Protozoa also showed UV-T synergistic effect (under illumination conditions), achieving 3-log reduction in 2-3 h at 44°C.
- The high similarity of the protozoon absorption spectrum to the DNA spectra demonstrated the negligible indirect endogenous photodamage and the existence of a few internal sensitisers.
- The model successfully responded to variations in the radiation spectra, confirming the insignificant inactivation experimentally observed for PET at temperatures below 40°C.
- The fact that thermal inactivation is almost the only possibility to inactivate protozoa in PET containers, the most used material for SODIS processes, is evidence of the need to look for alternative materials, such as PMMA or PP with UV-stabiliser.

Although protozoa show low susceptibility to external PPRI due to their resistant and thick wall, application of the model to field conditions may require

recalibration of the kinetic parameters to take into account specific substances present in the water that could reduce the efficacy by their role as radiation attenuators or, conversely, even improve the inactivation by acting as sensitisers for PPRI generation (this study was only carried out for bacterial inactivation in **Chapter III).**

3.6. Chapter VI: KINETIC MODELLING - BACTERIA: Mechanistic kinetic modelling of the thermal, photonic, and H_2O_2 addition effects

Bacteria are cell-based microorganisms with complex characteristics from the inactivation modelling point of view. In their metabolism, they generate ROS (H_2O_2, radicals, etc.) and contain several radiation absorbing components, such as DNA and enzymes that directly get altered by light, or substances that can act as photosensitisers generating more radicals that produce cell damage. Specifically, under solar UV illumination, DNA photon absorption leads to its modification, the internal photo-Fenton process occurs, their antioxidant enzymes (e. g. catalases and, to a lesser extent, superoxide dismutase) are deactivated, and the production of ROS increases. In addition, when *E. coli* are exposed in media rich in H_2O_2, this substance can permeate into the cell, raises the intracellular H_2O_2 level and, consequently, the production of radicals and cell damage. However, bacteria have mechanisms to repair photodamage and damage caused by radical attacks, being often able to recover and regrow in darkness after light exposure. The mathematical description of these advanced mechanisms results in complex kinetics that requires high computational power and expert knowledge to use it.

Chapter VI presents the development of a mechanistic kinetic model that considers the thermal and photonic effects on the solar disinfection of bacteria in H_2O_2-rich water. The results obtained in this chapter are discussed in detail in **Article 7** and **Article 8.**

Kinetic modelling steps

The kinetic analysis of the *E. coli* bacteria (model pathogen) inactivation enhanced with H_2O_2 was carried out by defining the significant reactions and estimating their kinetic parameters. **Table 3.6** and **Table 3.7** show the entire mechanism experienced by bacteria and H_2O_2, respectively.

Table 3.6: Mechanisms of the cell's respiration pathways and bacterial inactivation routes by radical's damage and thermal effect. In bold: kinetic parameters estimated in this work.

R.I	O_2 • generation	$O_2 + e^- \xrightarrow{NADH} O_2^{\cdot -}$	$r_1 = k_1'[NADH] = k_1$	k_1 = 5.4 • 10^{-6} M • s^{-1}
R.12	$O_2^{\cdot -}$ generation (light)	$NADH + O_2 \xrightarrow{h\nu} O_2^{\cdot -} + NAD^+ + H^+ + e^-$	$r12 = k_{12} \bullet I \bullet [NADH]$	$k_{12} = 1.07 \cdot 10^{-4}\ m^2 \cdot J^{-1}$
R.2	$O_2^{\cdot -}$ scavenging by SOD	$O_2^{\cdot -} + H^+ + SOD \rightarrow 1/2\, H_2O_2 + 1/2\, O_2$	$r_2 = k_2 \cdot [O_2^{\cdot -}][SOD]$	$k_2 = 10^9\ M^{-1}\ s^{-1}$
R.13	SOD deactivation	$SOD \xrightarrow{h\nu} SOD_i$	$r_{13} = k_{13} \cdot I \cdot [SOD]$	$k_{13} = 1.41 \cdot 10^{-7}\ m^2 \cdot J^{-1}$
R.3	H_2O_2 scavenging by CAT	$H_2O_2 + CAT \rightarrow 1/2\, O_2 + H_2O$	$r_3 = k_3[H_2O_2][CAT]$	$k_3 = 9 \cdot 10^5\ M^{-1}\ s^{-1}$
R.14	CAT deactivation	$CAT \xrightarrow{h\nu} CAT_i$	$r_{14} = k_{14} \cdot I \cdot [CAT]$	$k_{14} = 2.74 \cdot 10^{-5}\ m^2 \cdot J^{-1}$
R.4	Internal Fenton	$Fe^{2+} + H_2O_2 \rightarrow Fe^{3+} + HO^- + HO^{\cdot}$	$r_4 = k_4[Fe^{2+}][H_2O_2]$	$k_{0_4} = 8.21 \cdot 10^{11}\ M^{-1}\ s^{-1}$, $E_{a_4} = 4.9 \cdot 10^4\ J \cdot mol^{-1}$
R.5	Internal Fenton-like	$Fe^{3+} + Donor^{red} \rightarrow Fe^{2+} + Donor^{ox}$	$r_5 = k_5[Fe^{3+}]$	$k_5 = 8.433 \cdot 10^{-2}\ s^{-1}$
R.15	Internal Photo-Fenton	$Fe^{3+} + H_2O \xrightarrow{h\nu} Fe^{2+} + H^+ + HO^{\cdot}$	$r_{15} = k_{15} \cdot I \cdot [Fe^{3+}]$	$k_{15} = 3.92 \cdot 10^{-5}\ m^2\ J^{-1}$
R.6	Radical self-scavenging	$H_2O_2 + HO^{\cdot} \rightarrow O_2^{\cdot -} + H_2O + H^+$	$r_6 = k_6[H_2O_2][HO]$	$k_6 = 2.7 \cdot 10^7\ M^{-1}\ s^{-1}$
R.7	$O_2^{\cdot -}$ disproportionation	$2O_2^{\cdot -} + 2H^+ \rightarrow H_2O_2 + O_2$	$r_7 = k_7[O_2^{\cdot -}]^2$	$k_7 = 33.04\ M^{-1}\ s^{-1}$

R.8	$HO^{\cdot}$ recombination	$2\,HO \rightarrow H_2O_2$	$r_8 = k_8 \left[HO^{\cdot} \right]^2$	$k_8 = 4.6 \cdot 10^9\ M^{-1}\ s^{-1}$
R.9	Bacterial damage $O_2^{\cdot -}$	$B_i\ O_2^{\cdot -} \rightarrow B_{i+1}$	$r_9 = k_9 \left[O_2^{\cdot -} \right] \left[B_v \right]$	$n = 27$ $\quad k_9 = 33.1 M^{-1}\ s^{-1}$
R.10	Bacterial damage $HO^{\cdot}$	$B_i + HO^{\cdot} \rightarrow B_{i+1}$	$r_{10} = k_{10} \left[HO^{\cdot} \right] \left[B_v \right]$	$k_{r-ROS} = 10.8\ s^{-1}$ $\quad k_{10} = 5 \cdot 10^{-5}\ M^{-1}\ s^{-1}$
R.11	Thermal inactivation	$B_v \xrightarrow{T} B_i$	$r_{11} = k_{11}\,(T) \left[B_v \right]$	$k_{0_{11}} = 4.18 \cdot 10^{19}\ s^{-1}$ $E_{a_{11}} = 1.38 \cdot 10^5\ J \cdot mol^{-1}$
R.16-1	Direct damage (at 20°C)	$B_v \xrightarrow{h\nu} B_i$	$r_{16} \rightarrow k_{16}\,(I) \left[B \right]$	$m = 5, k_{R-RAD} = 1.75 \cdot 10^{-3}\ s^{-1},$ $k_{16} = 2.23 \cdot 10^{-4}\ m^2 \cdot J^{-1}$
R.16-2	Direct damage + T-UV synergy	$B_v \xrightarrow{h\nu,T} B_i$	$r_{16} = k_{16}\,(I,T) \left[B \right]$	$m = 5,\ k_{R-RAD} = 1.75 \cdot 10^{-3}\ s^{-1},$ $k_{0_{16}} = 4.16 \cdot 10^{-3}\ m^2 \cdot J^{-1},$ $E_{a_{16}} = 7.47 \cdot 10^3\ J \cdot mol^{-1}$

Table 3.7: Mechanism of the H2O2 decomposition and its consumption when added to water inoculated with *E. coli.* In bold: kinetic parameters estimated in this work.

R.A	H_2O_2 decomposition	$H_2O_{2ext} \xrightarrow{T} \frac{1}{2}O_2 + H_2O$	$r_A = k_A\left[H_2O_{2_{ext}}\right]$	$k_{0_A} = 3.95 \cdot 10^2\ s^{-1}$ $E_{a_A} = 4.48 \cdot 10^4\ J \cdot mol^{-1}$
R.B	H_2O_2 permeation	$H_2O_{2ext} \rightarrow H_2O_2$	$r_B = k_B\left(\left[H_2O_{2ext}\right] - \left[H_2O_2\right]\right)$	$k_B = 70\ s^{-1}$
R.C	Membrance-H_2O_2 interaction	$H_2O_{2ext} + B_v \rightarrow \frac{1}{2}O_2 + H_2O + B_v$	$r_C = k_C\left[B_v\right]\left[H_2O_{2ext}\right]$	$k_C = 2.04 \cdot 10^{10}\ M^{-1}\ s^{-1}$
R.D	OM killed cells-H_2O_2 interaction	$H_2O_{2ext} + OM_{red} \xrightarrow{T} OM_{ox}$	$r_D = k_D\left[OM_{red}\right]\left[H_2O_{2ext}\right]$	$k_{0_D} = 2.14 \cdot 10^7\ M^{-1}\ s^{-1}$ $E_{a_D} = 4.93 \cdot 10^4\ J \cdot mol^{-1}$ $\zeta = 3.63 \cdot 10^{11}$ OM/bacteria

Dark conditions

Kinetics parameters obtained with the RM-1 (shown in **Table 3.6** and **Table 3.7)** accurately reproduced the experimental data (NRMSLE=4.4% for bacteria and NRMSE= 12.9% for H_2O_2). The series-event model that reproduces the cell inactivation caused by radical's attacks (R.9 and R.10), is capable of developing profiles with curvilinear shape, being more curved for more events. However, in this case, the shape is linear due to the high value of the recovery constant (k_{R-ROS} = 10.8 s^{-1}), which straightens the curve (dashed yellow lines in **Fig. 3.15).** Due to the linear shape of disinfection profiles, a pseudo-first-order kinetic constant of each experiment was obtained to compare with that obtained experimentally. **Fig. 3.14** showcases the excellent agreement between the experimental and predicted data.

Fig. 3.14: Experimental and predicted pseudo first-order kinetic constant of the *E. coli* inactivation under dark conditions.

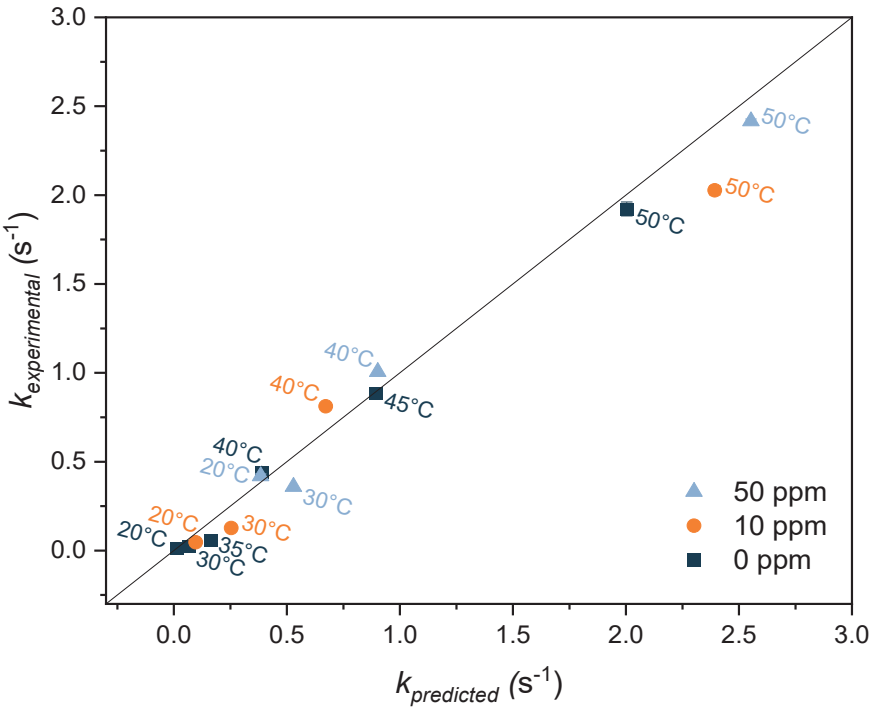

Illuminated conditions

Kinetics parameters obtained with the RM-2 and RM-3 (showed in **Table 3.6** and **Table 3.7)** successfully reproduced the effect of UV radiation and temperature on disinfection profiles (RM-2 NRMSLE=17.3% and RM-3 NRMSLE=14.0%). Despite the results in dark conditions, all the inactivation curves under UV illumination **(Fig. 3.15** and **Fig. 3.16)** showed the characteristic curved shape of the series-event model.

Fig. 3.15: Evolution of the *E. coli* concentration profiles depending on the UV irradiance Line: predicted data. Dots: experimental data.

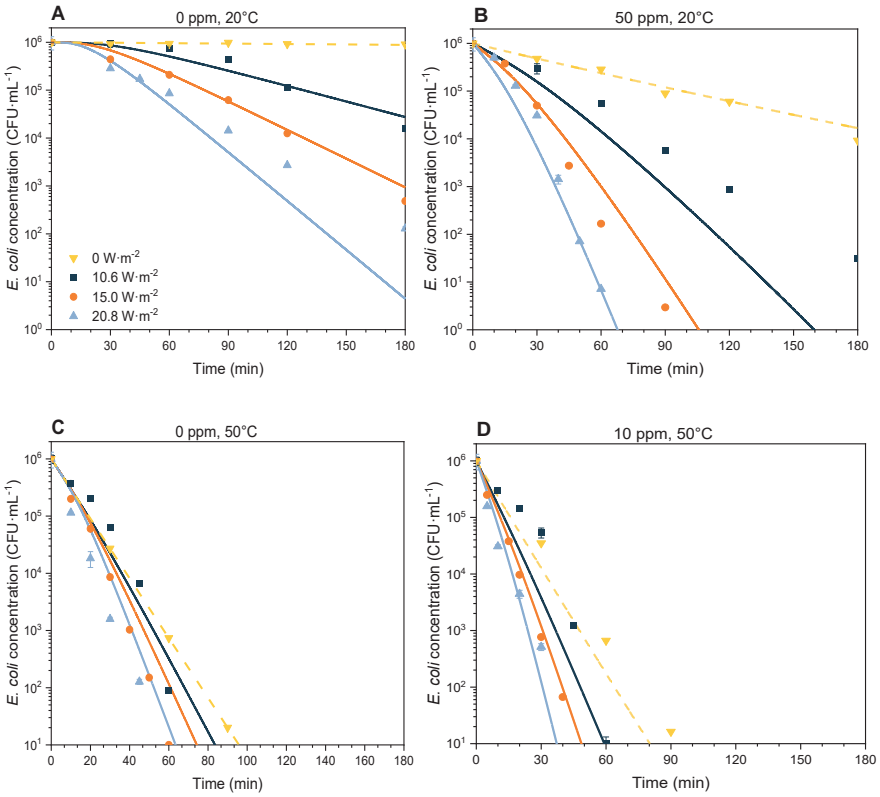

Fig. 3.16: Evolution of the *E. coli* concentration profiles depending on the initial H2O2 external concentration. Line: predicted data. Dots: experimental data.

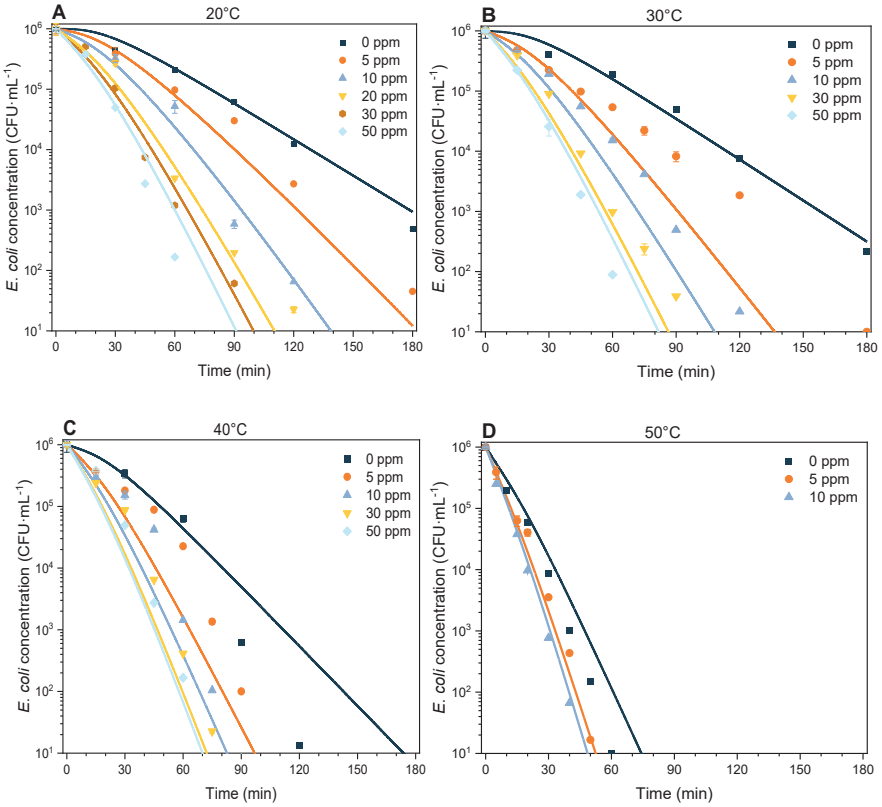

In this case, the low value of the photonic recovery constant ($1.75 \cdot 10^{-3}$ s^{-1}) is not capable of straightening the curve. The number of radicals' attacks (m = 27) is 5.5 times higher than the number of damage levels by the direct photonic process, confirming the critical effect produced by photons in comparison with radicals. In contrast, the recovery constant for radical damage is much lower than the solar one, but it must also go through a higher number of levels to completely heal the bacteria, resulting again in higher potential damage produced by light, probably because bacteria are used to radical attacks due to cell respiration and not to photonic damage.

Highlights of the estimated kinetic parameters values

One of the advantages of studying the effect of H_2O_2 on bacteria disinfection is the opportunity to understand the underlying mechanisms and the role of

internal substances (since H_2O_2 permeates into the cell), as well as to find reactions that do not play an important role, at least kinetically. **Fig. 3.17** shows the integrated mechanistic proposal (the reactions and their kinetic parameters can be found in **Table 3.6** and **Table 3.7).**

Fig. 3.17: Integrated mechanistic proposal for *E. coli* inactivation under the H_2O_2-enhanced inactivation process.

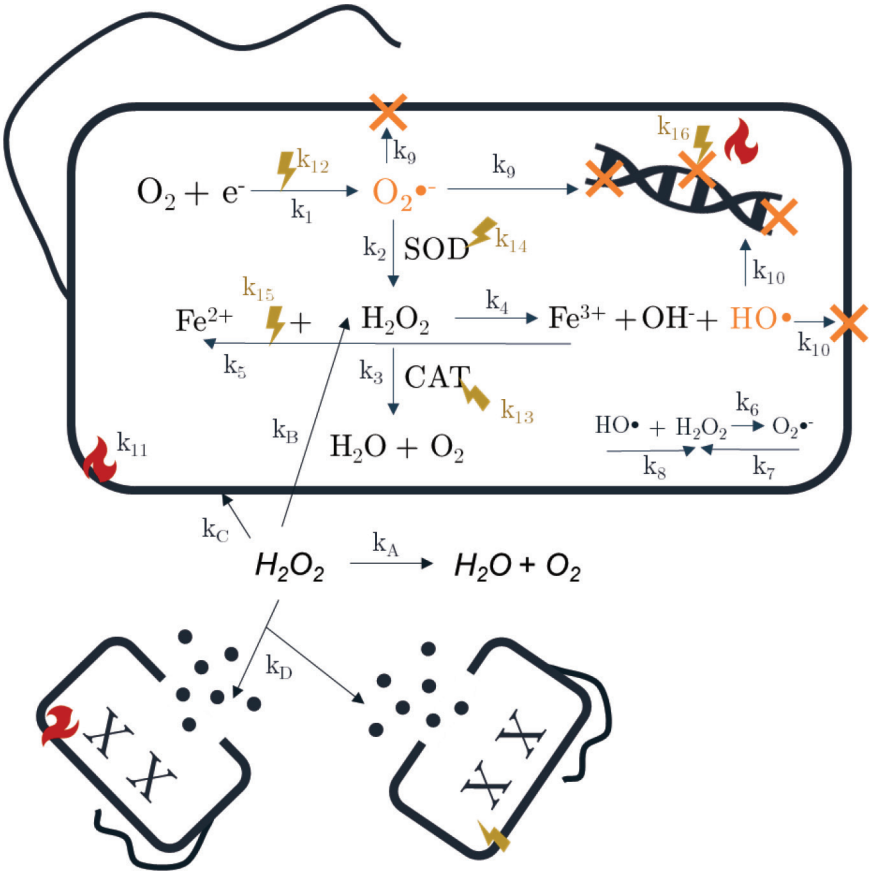

For example, the estimated values of the kinetic parameters agree with the *mode-one killing* cells by H_2O_2 (inactivation kinetic routes related to internal damage produced by radicals' attacks, it reaches its maximum around 1–2 mM H_2O_2 external concentration (Imlay and Linn, 1986)), confirming that not only growing cells follow the two killing modes, but also stationary phase cells.

Another characteristic of the *mode-one killing* is a low value of the Fe^{2+} recycling rate. Although Fenton oxidation rate in cells is higher than usual (k_4= 4400 $M^{-1}s^{-1}$ at 37°C (Park *et al.,* 2005), if the cell's potential to reduce Fe^{3+} to Fe^{2+} is also high,

then the concentration of Fe^{2+} would be constant, Therefore, the *mode-one killing-would* not exist (Uhl *et al.,* 2015). The obtained value for k_5 ($8.43 \cdot 10^{-2}$ s^{-1}) is low enough to guarantee the presence of Fe^{3+} under toxic levels of H_2O_2 and allows a decrease of Fe^{2+} concentration as the external H_2O_2 concentration rises.

Regarding the donor substance that performs the ferric to ferrous iron reduction, some authors suggest that $O_2^{\bullet-}$ or cysteine could be the reductant agent. During the oxidative process, the levels of $O_2^{\bullet-}$ lightly increase (the model simulations show that the amount of $HO^{\bullet}$ varies significantly with experimental conditions and over time, while $O_2^{\bullet-}$ concentration experiences small variations), raising the kinetic rate. However, $O_2^{\bullet-}$ is excluded since k_5 would take a value around 10^{-5} s^{-1} (rate constant 10^5 $M^{-1}s^{-1}$ (Bielski *et al.,* 1985) multiplied by the concentration IO^{-10} M, and that would not suffice for the iron pool. So, another suggestion is cysteine. Free cysteine is present in low concentrations to generate the strong DNA damage observed. It was previously found that when H_2O_2 is present, cysteine homeostasis is disrupted, and free cysteine storage increases around eightfold (Park and Imlay, 2003). Therefore, cysteine could be the donor species, being in a concentration between 0.1-2 mM in the cell (Park and Imlay, 2003), which implies a more reasonable pathway, having a kinetic constant around 40-800 $M^{-1}s^{-1}$.

In spite of the SOD photoinactivation that also occurs (reducing the rate of H_2O_2 formation), the photoinactivation of CAT prevails ($k_{14} \gg k_{13}$), reducing the H_2O_2 conversion and inadvertently increasing the H_2O_2 levels inside the cell.

Finally, the value of the activation energy is not very high (Ea_{SYN}= $7.47 \cdot 10^3$ J • mol^{-1}) which involved a value of ki_8 only 1.33 times higher at 50°C than at 20°C. In contrast, the activation energy for the bacterial thermal inactivation resulted in being higher (Ea_{11} = $1 \cdot 38 \cdot 10^5$ J • mol^{-1}) which implied a value of k_{11} almost 200 times higher at 50°C than at 20°C. Hence, the synergistic effect is not very significant for this specific bacterial strain and experimental conditions. Since this model should be optimised for each type of strain, we have decided to include the description of the synergy, allowing the possibility of considering this effect.

Effect of operational conditions on disinfection rate

Another particular strength of this mechanistic kinetic model is the capability of elucidating the best operational conditions for the process. To do so, the required solar exposure time to achieve a 99.99% of *E. coli* removal (t99.99%) has been obtained from the model's predictions **(Fig. 3.18).** It can be seen that temperatures above 50°C have a strong effect on bacterial inactivation, whereas the thermal effect at 20-30°C is negligible. If the thermal effect is not present (scenarios at 20°C), the illumination with solar light is necessary

to achieve inactivation times lower than 4 h (240 min). Even the addition of the highest H_2O_2 concentration (50 ppm) is not enough to require less than 6 h. Furthermore, if UV illumination and H_2O_2 addition are combined, the disinfection can be achieved in 50–120 min, and if the highest UV illumination or H_2O_2 dose (20.8 W • m^{-2} and 50 ppm) is used, the required time (50–90 min) is comparable to the required times at 50°C. At 40°C, the thermal effect contributes in the same way as the radiation and H_2O_2 and its combination resulted in required time between 50–90 min.

Fig. 3.18: Predictions of the required solar exposure time to achieve **99.99%** of bacteria removal.

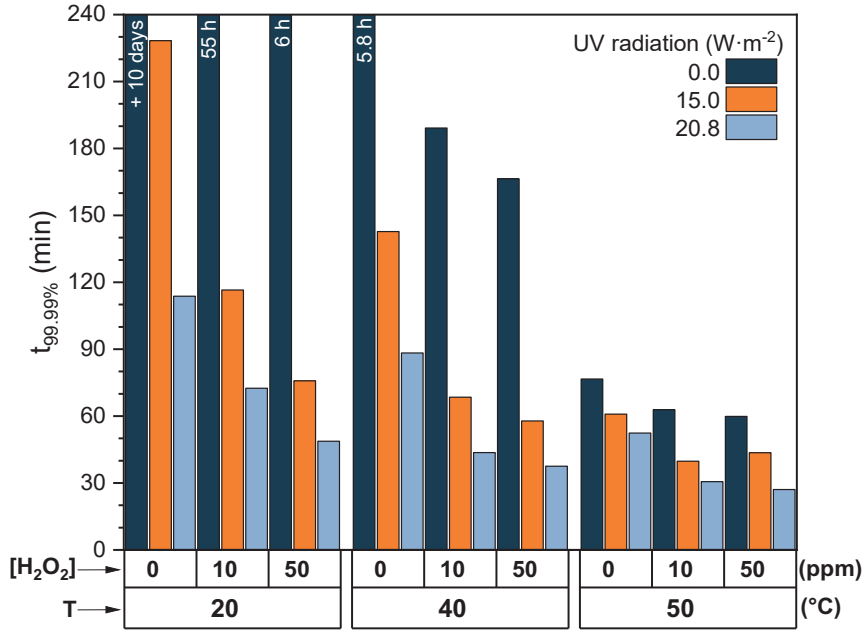

Final discussion

A novel comprehensive kinetic model for the *E. coli* bacteria inactivation enhanced with H_2O_2 has been developed as a function of water temperature, irradiance, and H_2O_2 concentration.

The study of the enhancement caused by H_2O_2 addition helped to elucidate the internal cellular mechanisms and their kinetic parameters, for example:

- Not only growing cells follow the two killing modes, but also stationary phase cells.

- Kinetic parameters suggest that cysteine can be the donor substance that performs the ferric to ferrous iron reduction during the internal Fenton process, and $O_2^{\bullet -}$ should be excluded since its concentration is not high enough to achieve the kinetic rate.

- The light-mediated SOD inactivation was found to be significantly lower (even negligible) than that for CAT.

- Cell components and remaining debris are the main sinks of ineffective consumption of the externally added H_2O_2.

Another particular strength of this mechanistic kinetic model is its capability to provide the best operational conditions for the process. The highlighted results are summarised as follows:

- Under dark conditions, at low temperature (20-30ºC) and under dark conditions, the thermal effect is negligible. The inactivation is led by radicals' damage, and it is demonstrated that the role of the $O_2^{\bullet -}$ 2in cell inactivation is significant, while externally added H_2O_2 is mainly consumed by the interaction with the cell's membrane and during/after its permeation. At 40°C, the contribution of the radicals' damage and the thermal on the bacteria inactivation is comparable. At high water temperatures (50°C), the inactivation (3-log reduction achieved in 80 min) is faster and strongly controlled by thermal inactivation, suggesting that even at high H_2O_2 concentrations, this pathway remains unchanged.

- Under illumination conditions, the potential damage produced by light was found higher than the radicals' one (even achieving 3-log reduction in 30 min), probably because bacteria are used to radical attacks due to cell respiration and not to photonic damage.

Finally, developing a mechanistic model for complex organisms such as bacteria complicates the account for all the variables involved in the SODIS process and increases computational costs and user efforts. For this reason, the influence of the radiation spectrum has not been included in this kinetic model. However, the complexity has helped to understand better the unknown bacteria pathways.

In this case, if the SODIS process is performed in PET containers, the model can be easily applied to field conditions applying the procedure developed in **Chapter III** to account for the effect of naturally occurring substances. For other materials, the recalibration of the kinetic parameters is recommended since sensitisers can be sensitive to UVB wavelengths which PET cuts.